Electronic Supplementary Material (ESI) for Journal of Materials Chemistry A.

Supporting Information

Enriched Nucleation Sites for Pt Deposition on Ultrathin WO_3 Nanosheets with Unique Interaction for Methanol Oxidation

Yiqiong Zhang,[+a] Yongliang Shi,[+b] Ru Chen,[+a]* Li Tao,[a] Chao Xie,[a] Dongdong Liu,[a] Dafeng Yan[a] and Shuangyin Wang[a]*

[a] State Key Laboratory of Chem/Bio-Sensing and Chemometrics, College of Chemistry and Chemical Engi-neering, Hunan University, Changsha, 410082, P. R.China.

[b] ICQD/Hefei National Laboratory for Physical Sciences at Microscale, and Key Laboratory of Strongly-Coupled Quantum Matter Physics, Chinese Academy of Sciences, and Department of Physics, University of Science and Technology of China, Hefei, Anhui 230026, P. R.China

* E-mail for S.W.: shuangyinwang@hnu.edu.cn, chenru@hnu.edu.cn

Experimental Section

Synthesis of bulk WO_3 nanosheets. In a typical synthesis, $Na_2WO_4 \cdot 2H_2O$ (2.0 g) and citric acid (1.2 g) were mixed together with 150 mL of distilled water in a beaker. After vigorous stirring for 10 min, several milliliters of 6 M hydrochloric acid aqueous solution was introduced into the aqueous solution (adjust the pH to ~1), resulting in a light yellow precipitation. After stirring for 30 min, the mixture was transferred into a 200 mL Teflon-lined stainless steel autoclave and reacted at 120 °C for 24 h. After the reaction completed, the resulting solid and solution were separated by centrifugation at 9600 rpm for 10 min and the collected solid was washed with distilled water and ethanol for several times to remove the ions possibly remaining in the final products, and finally dried in oven for 12 h.

Synthesis of ultrathin WO_3-Ar nanosheets. 20 mg of bulk WO_3 was spread on the quartz boat, and moved into the plasma reactor which is filled with Ar gas, then it was directly treated by plasma (commercial 13.56 MHz RF source) with power of 200 W and pressure of 40 Pa for 30 min. After that, the plasma treated samples were taken out from the plasma reactor and the color changed from light yellow to dark blue (named as WO_3-Ar). For comparison, 20 mg of bulk WO_3 were treated by plasma for 60 min with the same procedure.

Synthesis of Pt/WO_3-Ar hybrid nanostructures. In a typical synthesis, 80 mg WO_3-Ar nanosheets and 50 ml ethylene glycol were mixed together and stirred for 30 min. Then 0.5 ml sodium citrate (0.01 M) and 1.18 ml H_2PtCl_6 aqueous solution (20 mg ml^{-1}) were added to the above the mixture at room temperature and stirred for another 30 min. The resulting homogeneous mixture was transferred into three-necked flask, and the reduction of platinum was driven to completion by refluxing the solution at 140 °C for 6 h. After the reaction completed, the Pt/WO_3-Ar powders were collected by centrifugation at 11000 rpm for 15 min and washed with distilled water and ethanol for several times, then dried in a vacuum oven at 60 °C for 24 h.

Electrochemical Measurement. All of the electrochemical measurements were performed with a CHI 760D electrochemical workstation. The electrochemical activity of Pt/WO_3-Ar, Pt/WO_3, and commercial 10 wt.% Pt/C (Alfa Aesar Co., Inc) electrocatalysts was measured for the electro-oxidation of methanol. Generally, 4 mg of electrocatalyst sample was ultrasonically mixed in 1 mL of 2-propanol to form a homogeneous ink followed by dropping 15 μL of the electrocatalyst ink onto the surface of a glass carbon electrode (GCE). The diameter of GCE was 5 mm. Then, 1 μL of Nafion solution of 0.5% in isopropanol was added to fix the electrocatalysts on the GCE surface. A Pt wire and a saturated calomel electrode (SCE) were used as the counter and reference electrodes, respectively. All potentials in the present study were given versus SCE reference electrode. The electrochemical active area of Pt/WO_3-Ar, Pt/WO_3, and Pt/C electrocatalysts was measured in a nitrogen-saturated 0.5 M H_2SO_4 solution at a scan rate of 50 mV s^{-1}. The elelctrocatalytic activity for the methanol oxidation reaction was measured in a nitrogen-saturated 0.5 H_2SO_4 and 1.0 M CH_3OH solution at a scan rate of 50 mV s^{-1}. The tests were conducted at room temperature. The electrocatalytic activity of the Pt/WO_3-Ar toward CO oxidation was contrasted with Pt/WO_3 and Pt/C catalysts in 0.5 M H_2SO_4 electrolyte a scan rate of 10 mV s^{-1}. High purity CO was bubbled into the electrolyte solution for 6 min while keeping the electrode potential at -0.1 V to achieve maximum coverage of CO at the Pt centers. Dissolved CO was then purged out of the electrolyte by bubbling N_2 gas for 30 min. Since CO is an important intermediate product, its oxidation capability significantly influences the methanol oxidation reaction activity.

The electrochemically active surface area (ECSA) values of Pt/WO_3-Ar, Pt/WO_3, and Pt/C were calculated by measuring the charge from the CO adsorption peaks, with assumption that the smooth Pt electrode gives the CO adsorption a charge of 420 μC cm^{-2}, which represents the quantity of charge corresponding to the adsorption of a monolayer of CO on Pt site. The ECSA of Pt/WO_3-Ar, Pt/WO_3, and Pt/C were calculated using the formula below: [1]

$$\mathrm{ECSA}=\frac{Q_{co}}{420\times W_{Pt}}$$

where Q_{co} is the charge due to the CO adsorption in the CO stripping voltammograms (scan rate=10 mV s^{-1}), 420 μC cm^{-2} is the electrical charge associated with monolayer adsorption of CO on Pt site, and W_{Pt} is the loading of Pt catalyst on the working electrode.

Materials Characterization. The morphology and microstructure of all samples were investigated by transmission electron microscope (TEM, FEI, F20 S-TWIX). The actual Pt loadings in the catalysts was determined by inductively coupled plasma optical emission spectroscopy (ICP-OES, Spectro Blue Sop, German), Aqua regia was employed to dissolve Pt/WO_3 and Pt/WO_3-Ar (Because tungsten is insoluble in aqua regia, the content of tungsten cannot be measured). In detail, 0.1 g of the samples was completely dissolved into 20 ml aqua regia using a sonication bath for 30 min, then diluted in 50 ml bottle, and further took out 5 ml solution from the bottle and diluted it to 50 ml for the ICP-OES test. The size and thickness of electrocatalysts were determined by atomic force microscope (AFM, Brucker Bioscope system). The X-ray diffraction (XRD) measurements used a Rigaku D/MAX 2500 diffractometer with Cu Kα radiation. The Raman spectra were collected on a Raman spectrometer (Labram-010) using 532 nm laser. The X-ray photoelectron spectroscopic (XPS) measurements were carried out with an ESCALAB 250Xi using a monochromic Al X-ray source (200 W, 20 eV). The Electron paramagnetic resonance (ESR) measurements were carried out at a Bruker model A300 spectrometer.

DFT calculation details. Density functional theory (DFT) calculations are carried out with the Vienna Ab Initio Simulation Package (VASP).[2-4] The electron-nuclear interactions are described using projector augmented wave (PAW) method.[5] The Perdew-Burke-Ernzerhof (PBE) exchange-correlation functional[6] in generalized gradient approximation (GGA) scheme is employed in all calculations. The Kohn-Sham wave functions are expanded in plane waves up to a cutoff of 400 eV, and the convergence of the energies in the self-consistent step is achieved by use of a 10^{-6} eV threshold. For the slab calculations, the integration over the Brillouin zone is limited to the Γ point only. The WO_3 surface is modelled by (3×3) lateral surpercell with four O-W-O tri-layers. We use reconstruction[7, 8] and W-terminated surface to simulate the surface before and after Ar plasma etching. From the atomic structure of WO_3, we can see that it is more energy favourable to create oxygen vacancy on surface rather than internal part. Therefore, oxygen vacancy tend to gather on the surface. So W-terminated surface model is employed to simulate reduced WO_3 surface after Ar plasma etching. All of the atomic coordinates in $(Pt)_{20}/WO_3$ are relaxed. We have deposited Pt_{20} cluster on only one side of the slabs to mimic experimental situations. A vacuum of 15 Å and dipole correction[9] along the non-periodic direction are used, in order to mitigate the interlayer interaction. The structures were optimized until forces on relaxed atoms became less than 0.2 eV•Å^{-1}.

Supplementary Figures and Discussions

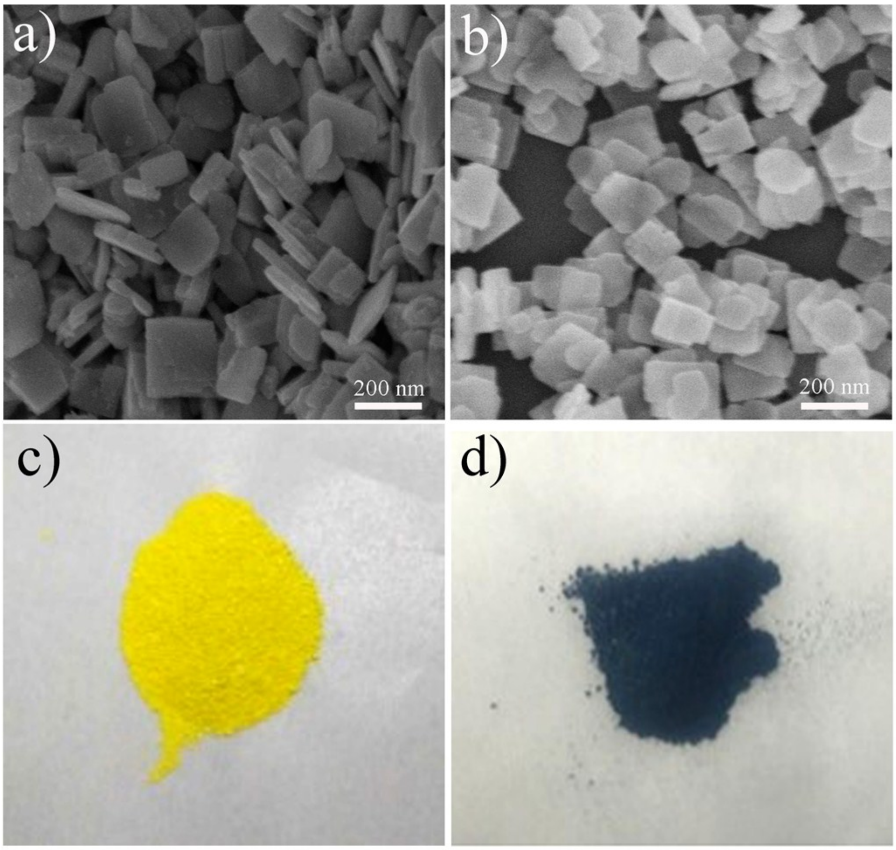

Figure S1. A SEM images and photograph of (a, c) the bulk WO_3, and (b, d) ultrathin WO_3-Ar product by Ar plasma exfoliation. After the exfoliation, the WO_3-Ar exhibits an intense blue color, while the color of the bulk WO_3 is light yellow. The blue color of tungsten oxides originates from a variety of oxygen-deficient stoichiometries.

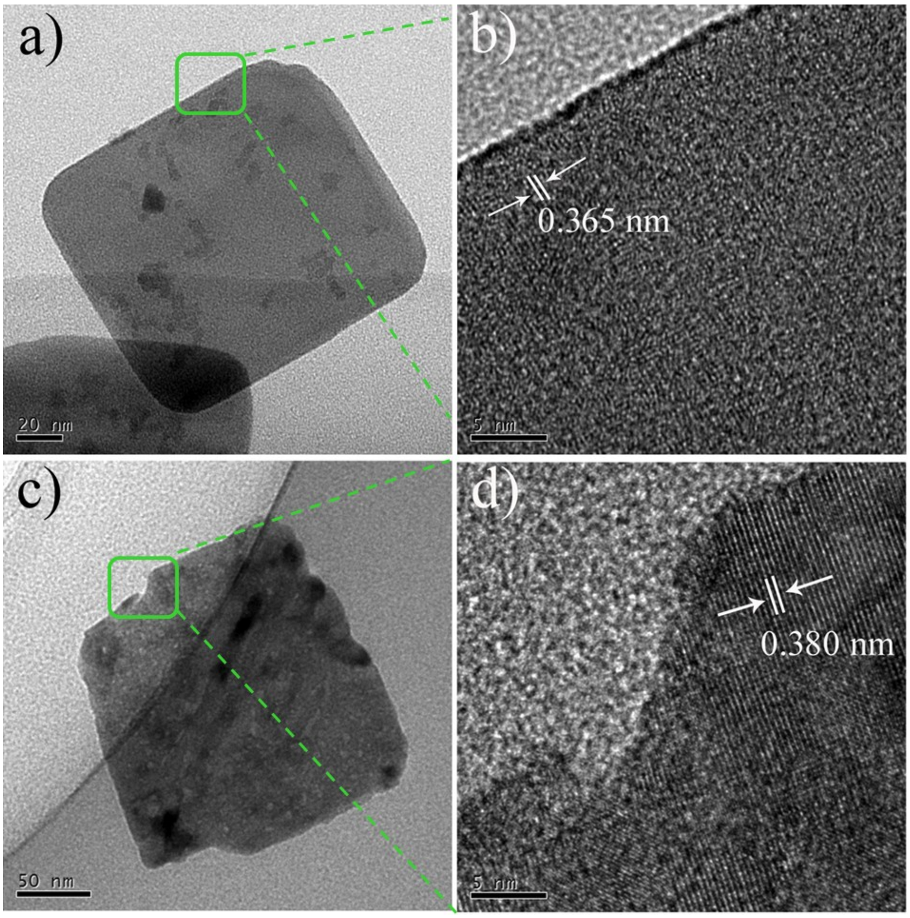

Figure S2. TEM and HRTEM images of bulk WO_3 nanosheets (a, b), and ultrathin WO_3-Ar nanosheets (c, d).

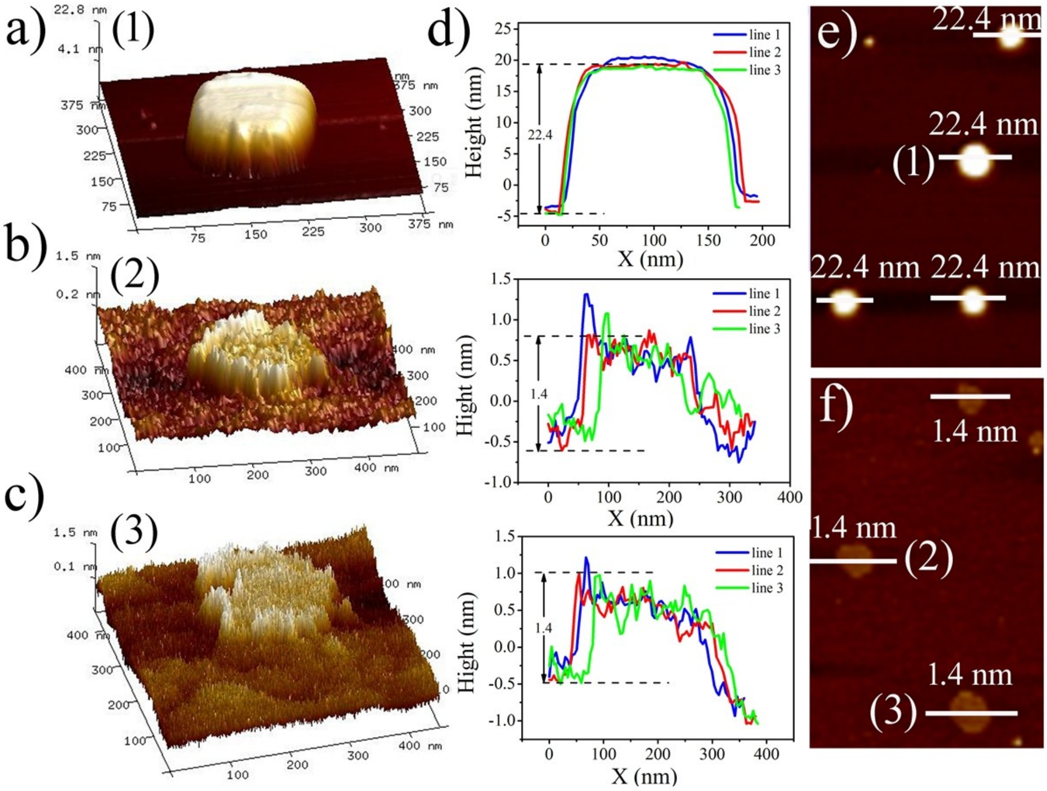

Figure S3. Atomic force microscopy (AFM) of bulk WO_3 (a, e) and ultrathin WO_3-Ar nanosheets (b, c, f), the corresponding height curves (d).

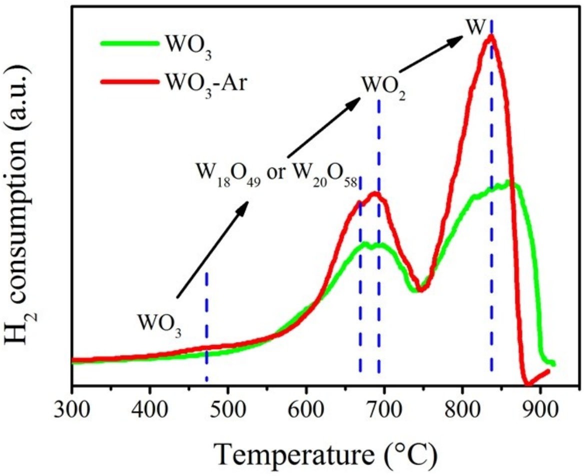

Figure S4. The temperature programmed reduction (TPR) of ultrathin WO_3-Ar nanosheets were studied in a H_2 (20%)-Ar flow (5 °C min^{-1}) at atmospheric pressure. The variation of H_2 consumption, as measured by the TCD signals, as a function of the temperature shows the reduction of WO_3 into W.

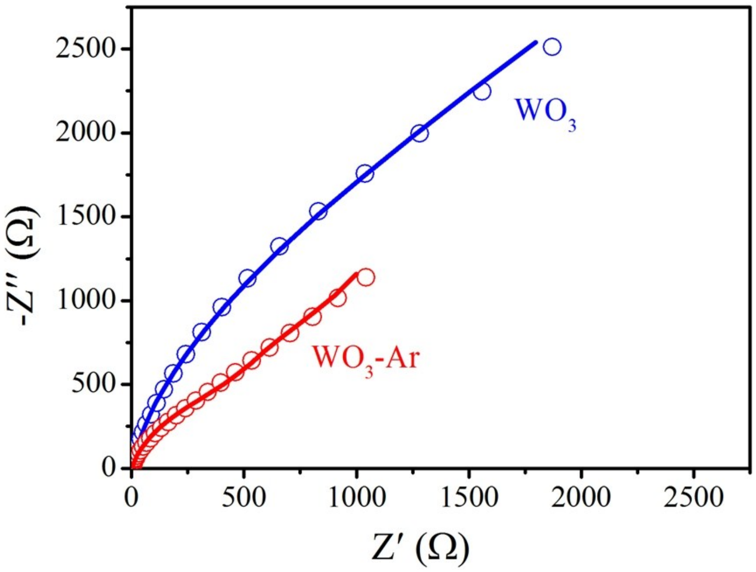

Figure S5. Electrochemical impedance spectroscopy (EIS) of ultrathin WO_3-Ar nanosheets and bulk WO_3 were employed from 100 kHz to 50 mHz at the open circuit potential (before any electrochemical cycling) in 0.5 M H_2SO_4 solution to investigate the conductivity, and charge transport of WO_3-Ar at the interface of WO_3-Ar/electrolyte. The open circles represent experimentally obtained data and the solid lines are the fit of the equivalent circuit.

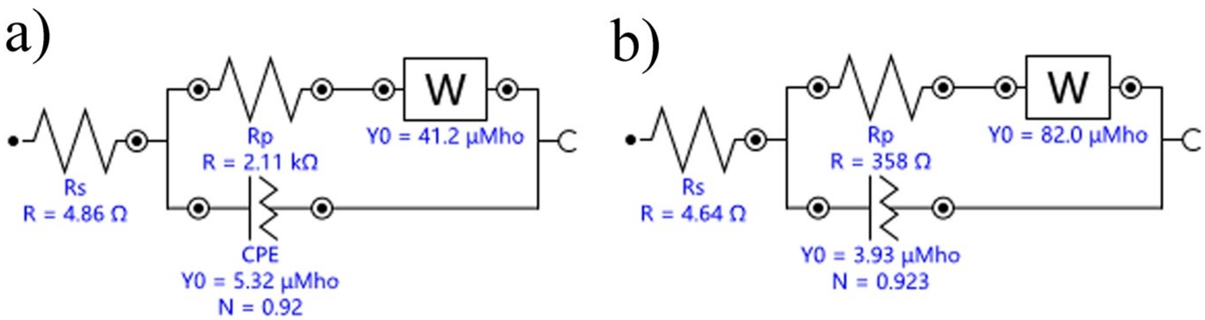

Figure S6. Electrochemical impedance spectroscopy (EIS) fitting results for (a) bulk WO_3 and (b) ultrathin WO_3-Ar nanosheets at the open circuit potential (before any electrochemical cycling). (Rs: electrolyte resistance, Rp: charge-transfer resistance, CPE: constant-phase element, W: Warburg Impedance.) According to the simulated parameter, the charge-transfer resistance (R_p) in WO_3-Ar electrode (358 Ω) is almost 6 times lower than that of bulk WO_3

(2110 Ω), revealing the easier charge (electron and proton) transfer at the interface of WO_3-Ar/electrolyte.

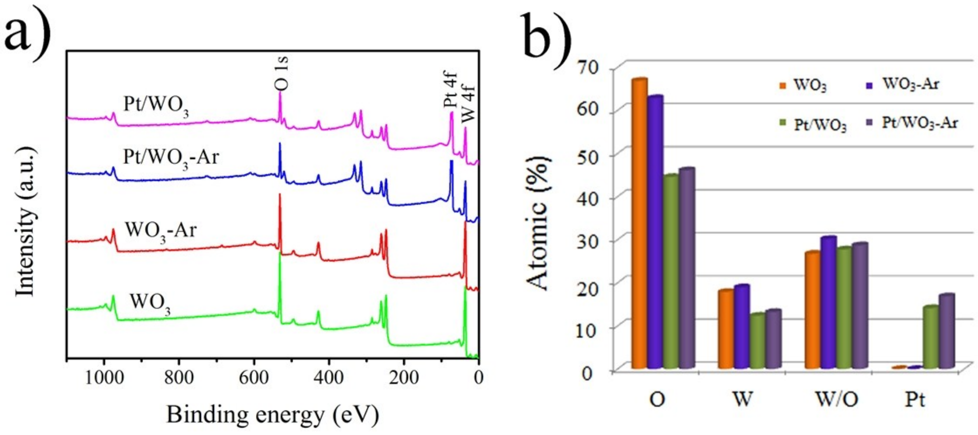

Figure S7. (a) XPS survey spectra of ultrathin WO_3-Ar nanosheets, Pt/WO_3-Ar, Pt/WO_3, and bulk WO_3, (b) Surface atomic percentage from the XPS of WO_3-Ar, Pt/WO_3-Ar, Pt/WO_3, and WO_3. The survey XPS indicates the presence of Pt, W, and O. For the ultrathin WO_3-Ar nanosheets, the oxygen percentage is smaller than that of the bulk WO_3, and the atomic ratio of W/O for WO_3-Ar also increases compared with bulk WO_3, indicating that the surface oxygen vacancies were generated by Ar plasma.

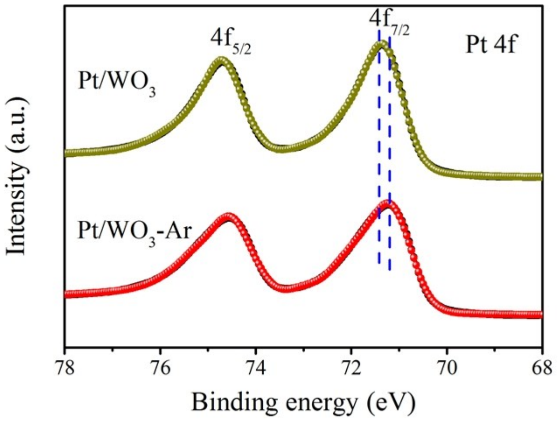

Figure S8. Pt 4f of Pt/WO_3 and Pt/WO_3-Ar hybrid nanostructures. The binding energy of Pt 4f for Pt/WO_3-Ar has a slight negative shift compared to that of the Pt/WO_3.

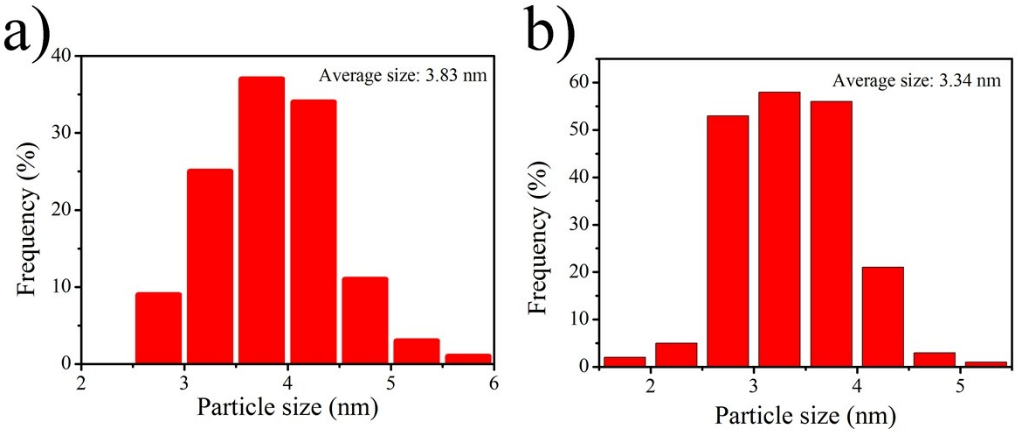

Figure S9. The Pt nanoparticles size of (a) Pt/WO_3 and (b) Pt/WO_3-Ar hybrids.

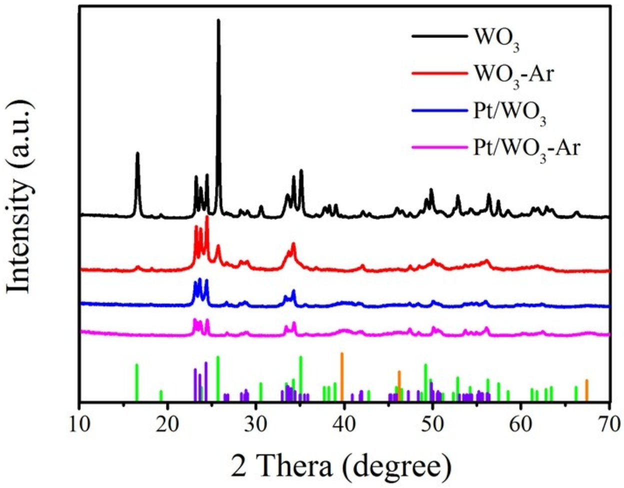

Figure S10. The XRD patterns of the WO_3, WO_3-Ar, Pt/WO_3 and Pt/WO_3-Ar samples. The green, purple, and orange line represent the the JCPDS Card of $WO_3 \cdot H_2O$ (PDF#43-0679), WO_3 (PDF#43-1035), and Pt (PDF#04-0802), respectively. As shown in Figure S10, all showing the typical diffraction peaks of WO_3 (PDF#43-1035). After the Ar plasma treatment, most of the diffraction peaks corresponding to the $WO_3 \cdot H_2O$ (PDF#43-0679) had disappeared, implying the loss of water molecules, which were etched by Ar plasma. In addition, for Pt/WO_3 sample, when Pt NPs were deposited on bulk WO_3 (belong to the $WO_3 \cdot H_2O$ phase) by the polyol thermal reduction method, the diffraction peaks of WO_3 corresponding to the $WO_3 \cdot H_2O$ had disappeared may implied the loss of water molecules during the thermal reduction reaction.

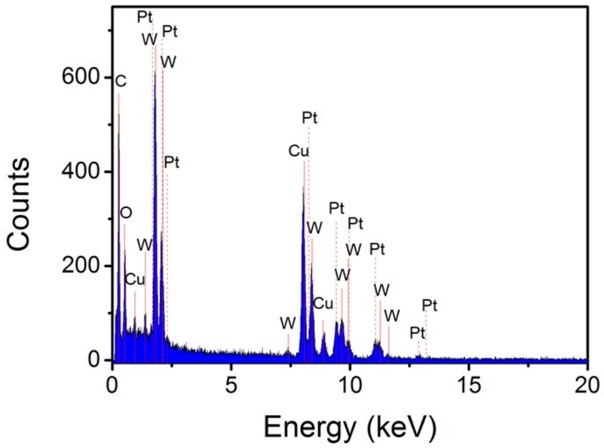

Figure S11. The EDX spectroscopy of the Pt/WO$_3$-Ar hybrids, which confirmed the existence of Pt, W, and O elements.

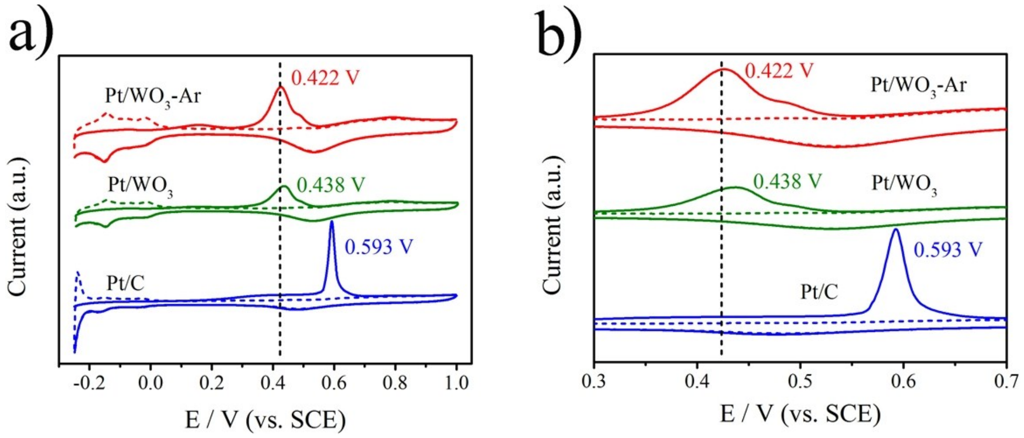

Figure S12. (a-b) CO stripping voltammograms of Pt/WO$_3$-Ar, Pt/WO$_3$, and Pt/C catalysts for 0.5 M H_2SO_4 solution (scan rate=10 mV s^{-1}). As shown in Figure S12(b), the CO peak potential (0.422 V) of Pt/WO$_3$-Ar shows a negative shift relative to Pt/WO$_3$ (0.438 V), which indicates that the Pt/WO$_3$-Ar with rich Vo exhibits better CO tolerance. Besides, both the CO peak potential of the Pt/WO$_3$-Ar and Pt/WO$_3$ are lower than that of the Pt/C, suggesting the bifunctional effect of WO$_3$ co-catalyst. Previous studies have demonstrated that the Pt/WO$_3$ catalyst exhibited much better CO tolerance than the Pt/C catalyst, which suggested the high CO tolerance should be attributed to the formation of a tungsten bronze compound.[10]

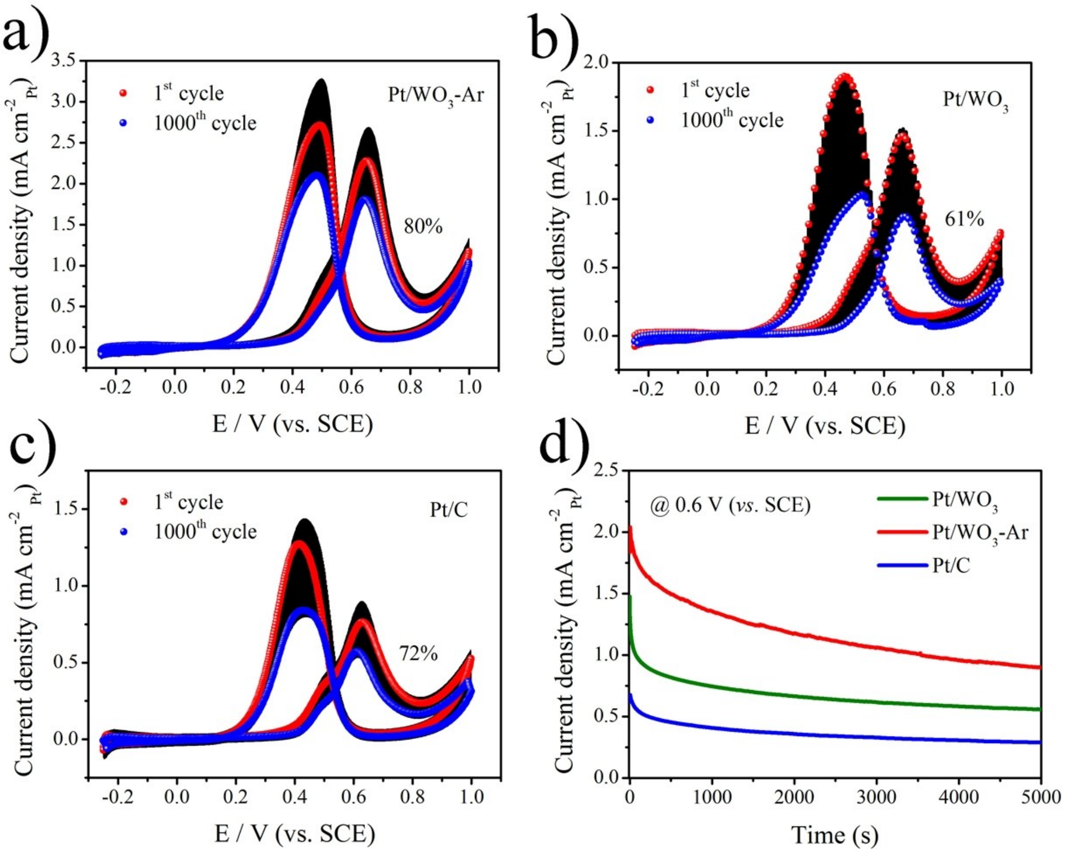

Figure S13. CVs of (a) Pt/WO_3-Ar, (b) Pt/WO_3, and (c) Pt/C catalysts from 1st to 1000th cycle in solution of 1 M CH_3OH and 0.5 M H_2SO_4 at 50 mV s^{-1}. After 1000 cycles, the conservation rate of peak current density is ~80% of the highest value, which indicated that Pt/WO_3-Ar catalyst has excellent cycling stability. However, Pt/WO_3 and Pt/C catalysts exhibit much lower conservation rates. (d) Chronoamperometry curves of Pt/WO_3-Ar, Pt/WO_3 and Pt/C catalysts were measured in 1 M CH_3OH and 0.5 M H_2SO_4 aqueous solution at 0.6 V (vs. SCE) to evaluate the rate of surface poisoning.

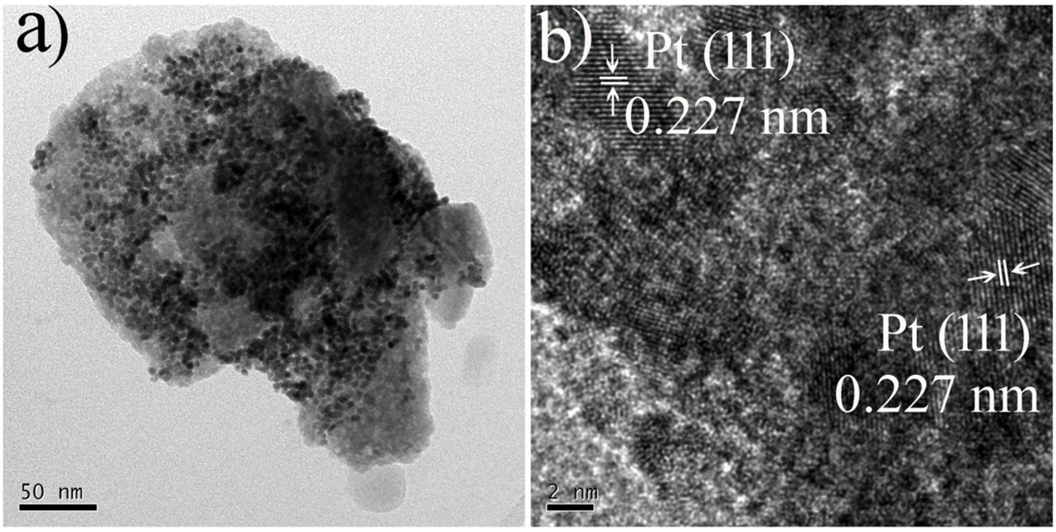

Figure S14. TEM and HRTEM images of Pt/WO_3-Ar after 1000 cycles. The surface morphologies of Pt/WO_3-Ar are retained well, indicating the high structural stability of Pt/WO_3-Ar.

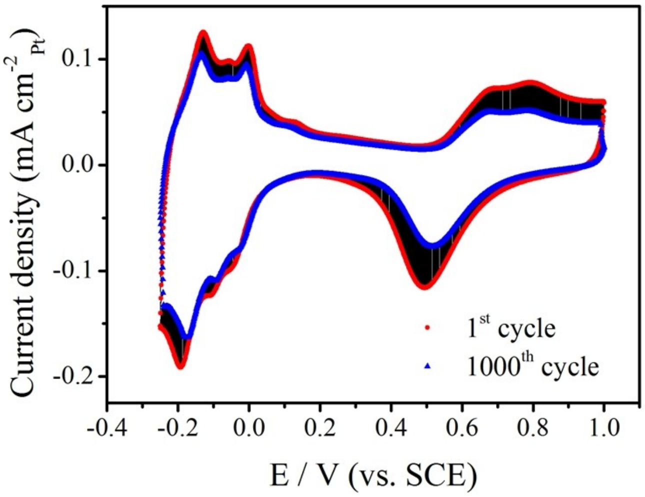

Figure S15. CVs of Pt/WO_3-Ar from first to 1000th cycle in N_2-saturated 0.5 M H_2SO_4 at 50 mV s^{-1}.

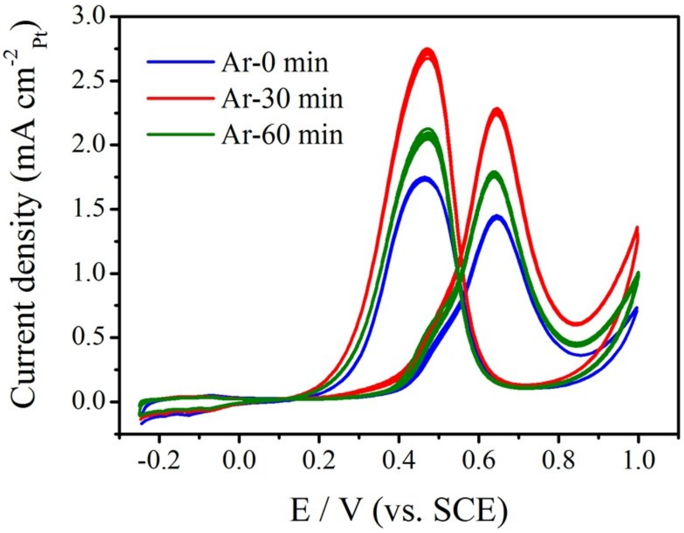

Figure S16. Cyclic voltammograms of Pt/WO_3-Ar with plasma treated the WO_3 naosheets by different time for 0 min, 30 min, and 60 min.

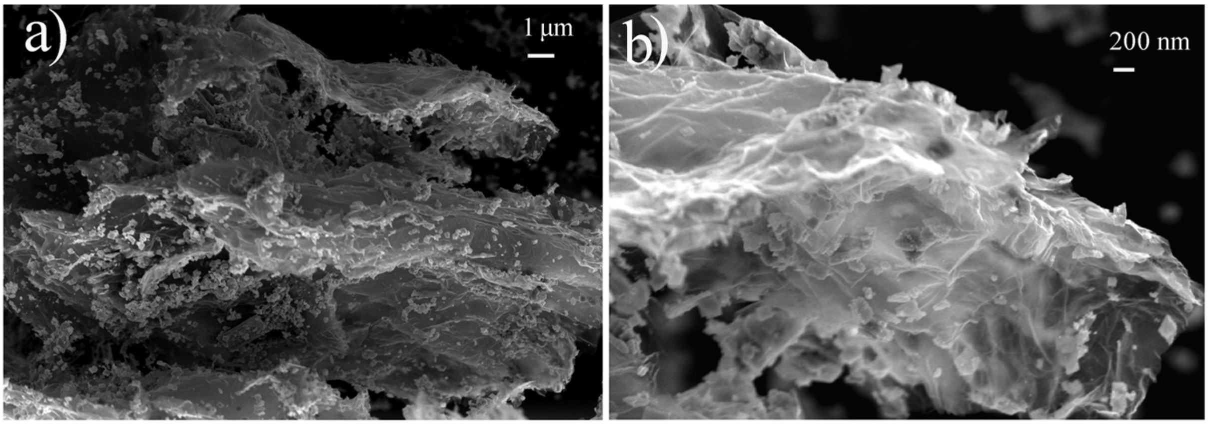

Figure S17. SEM images of the Pt/WO_3-Ar/G hybrid nanostructures. To further enhance the electrocatalytic activity for methanol oxidation, the Pt/WO_3-Ar catalyst was loaded onto graphene through a facile ultrasonic dispersion method (denoted as Pt/WO_3-Ar/G). The ultrathin Pt/WO_3-Ar nanosheets were anchored on the surface of the gauze-like graphene sheets, which can significantly improve the electronic transport.

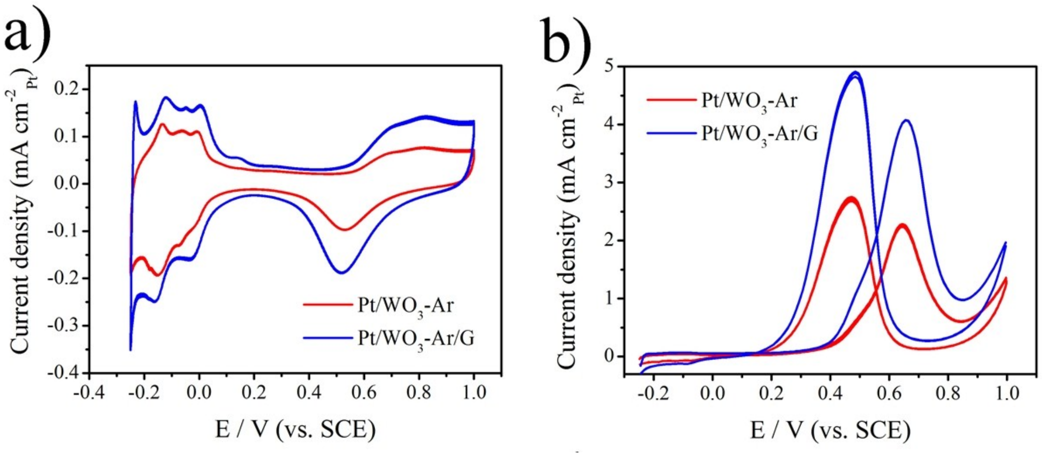

Figure S18. Cyclic voltammograms of Pt/WO$_3$-Ar and Pt/WO$_3$-Ar/G hybrids for (a) 0.5 M H_2SO_4 and (b) 1 M CH_3OH and 0.5 M H_2SO_4 solution.

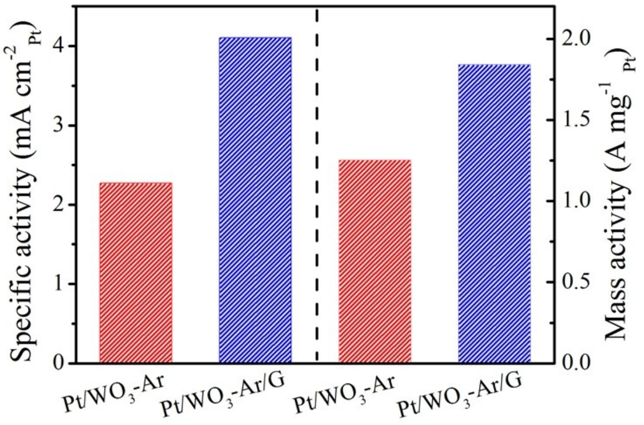

Figure S19. The specific activity and mass activity of Pt/WO$_3$-Ar and Pt/WO$_3$-Ar/G hybrids.

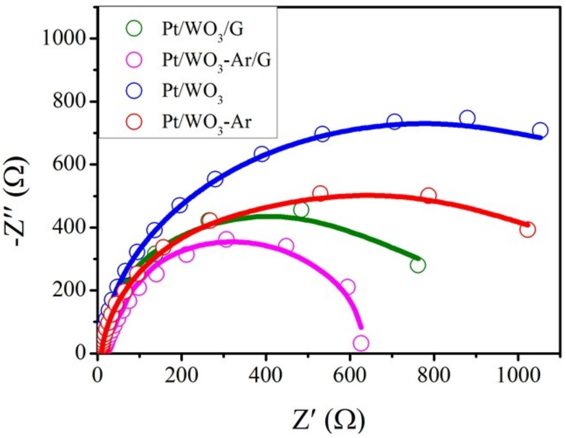

Figure S20. Electrochemical impedance spectroscopy (EIS) of Pt/WO$_3$-Ar/G, Pt/WO$_3$-Ar, Pt/WO$_3$/G and Pt/WO$_3$ catalysts were employed from 100 kHz to 50 mHz in the solution of 1 M CH$_3$OH+0.5 M H$_2$SO$_4$ at 0.4 V to investigate the charge transfer resistance of the catalysts/electrolyte interfaces, which is an important parameter to describe the electrocatalytic activity. The open circles represent experimentally obtained data and the solid lines are the fit of the equivalent circuit. A smaller diameter indicates a lower charge transfer resistance for the reaction and higher electrocatalytic activity.

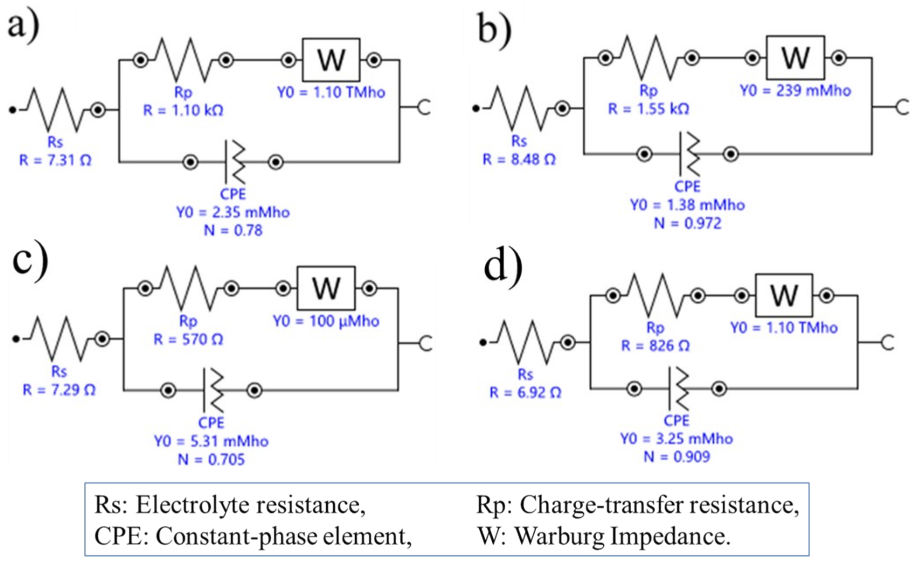

Figure S21. Electrochemical impedance spectroscopy (EIS) fitting results for (a) Pt/WO$_3$-Ar, (b) Pt/WO$_3$, (c) Pt/WO$_3$-Ar/G, and (d) Pt/WO$_3$/G catalysts. According to the simulated parameter, the charge-transfer resistance (R_p) in Pt/WO_3-Ar electrode is lower than that of Pt/WO_3 electrode, revealing the faster kinetics of methanol oxidation on Pt/WO_3-Ar and confirms the higher electrocatalytic activity of Pt/WO_3-Ar compared to the Pt/WO_3. Moreover, the Rp in Pt/WO_3-Ar/G and Pt/WO_3/G electrode is lower than that of Pt/WO_3-Ar and Pt/WO_3 electrode, respectively, which indicates that the addition of graphene can further improve the electrical conductivity.

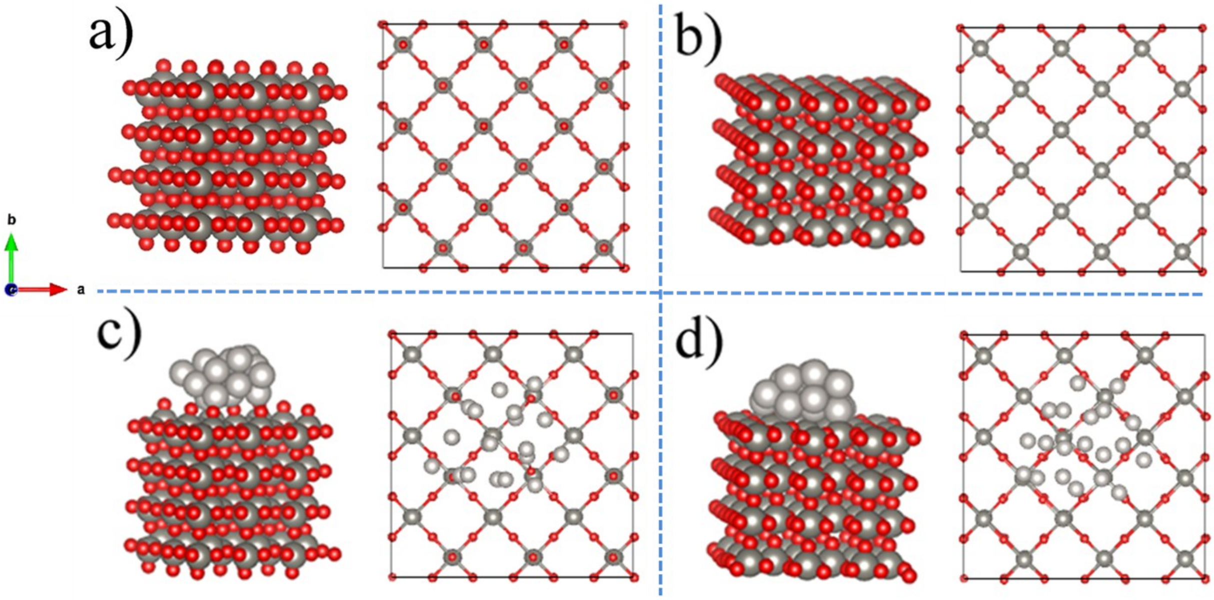

Lattice parameters
a = 16.05870 Å α = 90.0000°
b = 16.18320 Å β = 90.0000°
c = 31.55040 Å γ = 90.0000°
Unit-cell volume = 8199.3550 Å^3

Figure S22. Optimized structure and the top view of (a) stoichiometric reconstructed surface and (c) atomic structure of supported Pt_{20}. Optimized structure of (b) reduced W-terminated surface and (d) atomic structure of supported Pt_{20}. We use stoichiometric reconstructed and reduced W-terminated surface to simulate the surface before and after Ar plasma etching. Because the supported metal cluster over several nm, tend to form face-centered cubic (FCC) stacking.[11] Therefore, we deposit Pt_{20} cluster with FCC stacking as initial structure on one side of the slabs to mimic experimental situations.

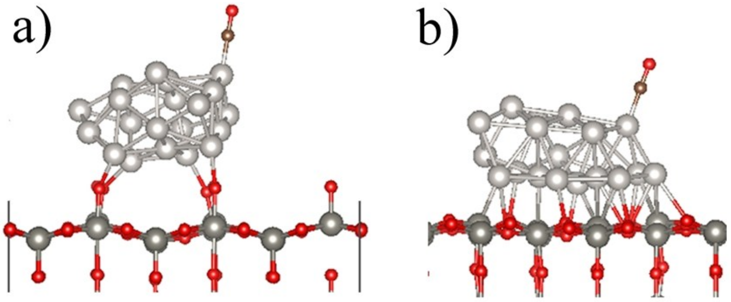

Figure. S23. Crystal structure of (a) the adsorption CO on Pt_{20} by supported O-terminated reconstructed WO_3, and (b) the adsorption CO on Pt_{20} by supported W-terminated WO_3. To explore the nature of anti-poisoning of CO in these two system, we check the binding strength of CO with Pt_{20} by adsorption energy of CO:

$$E_{ad} = E_{CO+(Pt)_{20}+WO_3} - E_{(Pt)_{20}+WO_3} - E_{CO}$$

where $E_{CO+\ (Pt)_{20}+WO_3}$ is total energy CO adsorbed on $(Pt)_{20}/WO_3$ heterostructure in the optimum geometry, $E_{(Pt)_{20}+WO_3}$ is energy of $(Pt)_{20}/WO_3$ and E_{CO} is energy of a single CO molecular.

Table S1. Detection of the actual Pt loadings in the catalysts by ICP-OES analysis.

Catalysts	**Pt (wt%)**
Pt/WO_3	9.6
Pt/WO_3-Ar	10.1

Table S2. The comparisons of some as-reported Pt-based electrocatalysts for MOR.

Catalysts	**Specific activity ($mA\ cm^{-2}\ _{Pt}$)**	**Mass activity ($A\ mg^{-1}\ _{Pt}$)**	**Reference**
Pt/WO_3-Ar	2.27	1.25	This work
Pt/WO_3	1.44	0.48	This work
Pt/WO_3 microphares	N/A	0.584	12
Pt/P-MCNTs	1.56	1.06	13
Pt/TiO_2 nanotubes	~1.65	>1	14
Pt/CeO_2/PANI THNRAs	N/A	0.361	15
Pt/MoO_2@C	N/A	0.57	16
Pt-Ni NFs/C	2.19	1.04	17
PtZn/MWNT	~1.08	~0.612	18
SnNiPt NPs	1.41	0.989	19
PtRu/CuNWs	1.60	0.45	20
PtCo NWs	1.95	1.02	21
Mesoporous-Pt/WO_3	N/A	0.706	22
Pt/$W_{18}O_{49}$	1.14	0.806	23
Pd@PtNi nanoplates	0.957	0.782	24
PtCo/C	1.70	0.83	25

Supporting References

1. C. C. Kung, P. Y. Lin, Y. Xue, R. Akolkar, L. Dai, X. Yu and C. C. Liu, *J. Power Sources*, 2014, **256**, 329-335.
2. G. Kresse and J. Hafner, *Phys. Rev. B Condens Matt.*, 1993, **48**, 13115-13118.
3. G. Kresse and J. Furthmüller, *Phys. Rev. B*, 1996, **54**, 11169-11186.
4. G. Kresse and J. Furthmüller, *Comp. Mater. Sci.*, 1996, **6**, 15-50.

5. G. Kresse and D. Joubert, *Phys. Rev. B*, 1999, **59**, 1758-1775.
6. J. P. Perdew, K. Burke and M. Ernzerhof, *Phys. Rev. Lett.*, 1996, **77**, 3865-3868.
7. F. Wang, C. Di Valentin and G. Pacchioni, *J. Phys. Chem. C*, 2012, **116**, 10672-10679.
8. M. Li, E. I. Altman, A. Posadas and C. H. Ahn, *Surf. Sci.*, 2003, **542**, 22-32.
9. L. Bengtsson, *Phys. Rev. B*, 1999, **59**, 12301-12304.
10. X. Cui, L. Guo, F. Cui, Q. He and J. Shi, *J. Phys. Chem. C*, 2009, **113**, 4134-4138.
11. Y. Shi, B. Song, R. Shahbazian-Yassar, J. Zhao and W. A. Saidi, *J. Phys. Chem. Lett.*, 2018, **9**, 2972-2978.
12. R. Ganesan and J. S. Lee, *J. Power Sources*, 2006, **157**, 217-221.
13. Z. Liu, Q. Shi, F. Peng, H. Wang, R. Zhang and H. Yu, *Electrochem. Commun.*, 2012, **16**, 73-76.
14. B. Abida, L. Chirchi, S. Baranton, T. W. Napporn, H. Kochkar, J.-M. Léger and A. Ghorbel, *Appl. Catal. B: Environ.*, 2011, **106**, 609-615.
15. H. Xu, A.-L. Wang, Y.-X. Tong and G.-R. Li, *ACS Catal.*, 2016, **6**, 5198-5206.
16. J. J. Zhang, X. L. Sui, G. S. Huang, D. M. Gu and Z. B. Wang, *J. Mater. Chem. A*, 2017, **5**, 4067-4074.
17. J. Ding, L. Bu, S. Guo, Z. Zhao, E. Zhu, Y. Huang and X. Huang, *Nano Lett.*, 2016, **16**, 2762-2767.
18. Z. Qi, C. Xiao, C. Liu, T. W. Goh, L. Zhou, R. Maligal-Ganesh, Y. Pei, X. Li, L. A. Curtiss and W. Huang, *J. Am. Chem. Soc.*, 2017, **139**, 4762-4768.
19. H. Fang, Y. Chen, M. Wen, Q. Wu and Q. Zhu, *Nano Res.*, 2017, **10**, 3929-3940.
20. J. Zheng, D. A. Cullen, R. V. Forest, J. A. Wittkopf, Z. Zhuang, W. Sheng, J. G. Chen and Y. Yan, *ACS Catal.*, 2015, **5**, 1468-1474.
21. L. Bu, S. Guo, X. Zhang, X. Shen, D. Su, G. Lu, X. Zhu, J. Yao, J. Guo and X. Huang, *Nat. Commun.*, 2016, **7**, 11850.
22. X. Cui, J. Shi, H. Chen, L. Zhang, L. Guo, J. Gao and J. Li, *J. Phys. Chem. B*, 2008, **112**, 12024-12031.
23. F. Li, H. Gong, Y. Wang, H. Zhang, Y. Wang, S. Liu, S. Wang and C. Sun, *J. Mater. Chem. A*, 2014, **2**, 20154-20163.
24. Y. Yan, H. Shan, G. Li, F. Xiao, Y. Jiang, Y. Yan, C. Jin, H. Zhang, J. Wu and D. Yang, *Nano Lett.*, 2016, **16**, 7999-8004.
25. L. Liu, E. Pippel, R. Scholz and U. Gösele, *Nano Lett.*, 2009, **9**, 4352-4358.